JOURNAL OF GEOPHYSICAL RESEARCH, VOL. 106, NO. D18, PAGES 20,811–20,819, SEPTEMBER 27, 2001

Aerosol optical depth measurements during the Aerosols99 experiment

Kenneth J. Voss,[1] Ellsworth J. Welton,[2] Patricia K. Quinn,[3,4]
Robert Frouin,[5] Mark Miller,[6] and R. Michael Reynolds[6]

Abstract. The Aerosols99 cruise took place during the period from January 14 to February 8, 1999, on the R/V *Ronald Brown*. The cruise track was almost a straight line in the southeast direction from Norfolk, Virginia, to Cape Town, South Africa, and afforded the opportunity to sample several different aerosol regimes over the North and South Atlantic. Handheld sunphotometers, a shadowband radiometer (FRSR), and a LIDAR were used to measure the aerosol optical depth (AOD) during the cruise. The AOD and angstrom exponent α (spectral dependence of the AOD) varied strongly between regimes. Maritime regions typically had AOD (500 nm) of approximately 0.10 ± 0.03, with α around 0.3 ± 0.3. An African dust event was encountered in which the AOD (500 nm) averaged 0.29 ± 0.05 with an α of 0.36 ± 0.13. At the Intertropical Convergence Zone (ITCZ), no measurements were obtained because of cloudiness; however, after the ITCZ we encountered a biomass burning aerosol with high average AOD (500 nm) of 0.36 ± 0.13, and a high α (0.88 ± 0.30). Farther south the aerosol went back to the low levels of a typical marine aerosol.

1. Introduction

The Aerosols99 cruise took place during the period from January 14 to February 8, 1999, on the R/V *Ronald Brown*, and on a cruise track from Norfolk, Virginia, to Cape Town, South Africa. This track afforded the opportunity to sample several different aerosol regimes over the North and South Atlantic. A suite of chemical and optical instrumentation was used during this cruise to measure the physical, chemical, and optical properties of the aerosols over this region. This data set shows an example of the aerosol regimes which may be sampled, but the aerosols are highly variable spatially and temporally.

There were many different instruments making measurements of the spectral aerosol optical depth (AOD) during this cruise. Three groups used Microtops sunphotometers (Solar Light Co., Philadelphia, Pennsylvania): the Brookhaven National Laboratory (BNL), the Pacific Marine Environmental Laboratory (PMEL), and the University of Miami group used a Microtops on this leg supplied by the SIMBIOS [*Mueller et al*., 1998] instrument pool. The Microtops sunphotometers are handheld instruments, which, when manually aimed at the Sun, make measurements of the direct solar irradiance to derive the AOD. There was another combination sunphotometer and radiometer, the Simbad instrument (manufactured by the University of Lille) operated by a group from Scripps which was also manually operated, and for the AOD measurements was operated in the same way as the Microtops instruments. BNL also had a FRSR shadowband radiometer on board [*Reynolds et al*., 2001]. This instrument operates automatically throughout the day making measurements of the indirect and direct solar irradiance which are individually averaged at 2-min intervals. Finally, there was a Micropulse LIDAR operating continuously (except at high noon) throughout this cruise making vertical profiles of the backscattering/attenuation profile at 1-min intervals. Each of these instruments has distinct advantages and disadvantages.

To measure the AOD with a radiometer, there must be a cloud-free line of sight to the Sun. Since the handheld instruments (Microtops and Simbad radiometer) are manually operated, the operator can select cloud-free periods to perform the measurements, visually avoiding cloud contamination. However, the need for an operator results in fewer measurements than is possible with an automated instrument. The FRSR takes measurements throughout the day automatically, thus any cloud-free periods during the day will be sampled. However, since there is no operator continually monitoring the measurements, algorithms must be developed to screen the processed data for cloudy periods (described in section 2.3). The calibrated Micropulse LIDAR (MPL) allows measurements of the boundary layer AOD even during periods of cirrus clouds. In addition, since this is an active measurement, the AOD can also be measured during the night, while all the other methods require the Sun. However, this method also requires an algorithm to avoid periods of lower-level clouds and requires a clean, aerosol-free layer be defined above the aerosol. The MPL also only supplies the AOD at one wavelength, thus there is no information on the spectral variation of the AOD.

In this paper we will present an overview of the methods used to obtain the AOD with each of these instruments. In addition, we will look at how the AOD and the spectral vari-

[1]Department of Physics, University of Miami, Miami, Florida.
[2]Goddard Earth Science and Technology Center, University of Maryland, Baltimore, Maryland.
[3]Pacific Marine Environmental Laboratory, NOAA, Seattle, Washington.
[4]Joint Institute for the Study of Atmosphere and Ocean, University of Washington, Seattle, Washington.
[5]Scripps Institution of Oceanography, University of California, San Diego, La Jolla, California.
[6]Environmental Sciences Department, Brookhaven National Laboratory, Upton, New York.

Paper number 2000JD900783.
0148-0227/01/2000JD900783$09.00

ation of the AOD was influenced by the different aerosol regimes sampled during this cruise. Other associated papers will look at the relationship between the AOD and surface measured aerosol properties [*Quinn et al*., this issue] and at the vertical profile information from the LIDAR [*Voss et al*., this issue].

2. Methods

There are a few definitions, which are common to all the measurements, that can be detailed first. The AOD is defined as the attenuation for a vertical path through the atmosphere due to the aerosols and is a portion of the total optical depth. The total optical depth τ is defined as

$$\tau = -\frac{1}{m}\ln\left(\frac{E}{E_o}\right), \tag{1}$$

where E_o is the extraterrestrial solar irradiance (solar irradiance that would be measured in the absence of an atmosphere), E is the surface measured direct solar irradiance, and m is the air mass or relative path length over which the measurement was performed. The parameter m is related to the solar zenith angle θ_s and at small solar zenith angles ($<80°$) is equal to $1/\cos(\theta_s)$. Note at zenith angles greater than 80°, because of the effect of Earth curvature, the relationship between solar zenith angle and air mass is more complicated [*Kasten and Young*, 1989].

Once τ is determined, the AOD can be determined by subtracting the contributions to τ from molecular scattering (Rayleigh scattering, τ_R) [*Penndorf*, 1957; *Bucholtz*, 1995] and molecular absorption. The spectral regions measured are usually chosen to avoid regions of strong molecular absorption (including water vapor), but the broad Chappius band absorption of O_3 requires that corrections be made for O_3 absorption [*Shaw*, 1979]. Once O_3 absorption τ_{O_3} is determined, the AOD is defined as

$$\mathrm{AOD} = \tau - \tau_R - \tau_{O_3}. \tag{2}$$

These parameters vary with the wavelength of light, hence the measurement wavelength must be taken into account. The spectral variation of the AOD can be characterized by the angstrom exponent α, defined as [*Angstrom*, 1964]:

$$\alpha = -\frac{\ln\left(\frac{\mathrm{AOD}(\lambda_1)}{\mathrm{AOD}(\lambda_2)}\right)}{\ln\left(\frac{\lambda_1}{\lambda_2}\right)}, \tag{3}$$

where λ_1 and λ_2 are two measurement wavelengths. The value of α is related to the size distribution of the aerosol; small values imply a low spectral variation and large particles, and large α implies high spectral variation and more smaller particles. AOD is a total column value, thus α derived from the AOD is determined by the column-averaged aerosol size distribution. Details of the specific instrumentation and the methods used to calibrate and reduce the data from these instruments will now be described.

2.1. Microtops

The five-channel handheld Microtops sunphotometer (Solar Light Co.) used by NOAA PMEL operated at 380, 440, 500, 675, and 870 nm. The spectral band pass of each filter (full width at half maximum (FWHM)) is 2 nm for the 380 nm channel and 10 nm for the other channels. The full angular field of view is 2.5°. The instrument has built-in pressure and temperature sensors and was operated with a GPS connection to obtain position and time of the measurements. A MATLAB routine, also used by the NASA SIMBIOS program and Brookhaven National Laboratory, was used to convert the raw signal voltages from the Microtops to AOD. Included in the conversion is a correction for Rayleigh scattering [*Penndorf*, 1957; *Buchlotz*, 1995], ozone optical depth, and an air mass that accounts for the Earth's curvature [*Kasten and Young*, 1989]. Ozone column amounts used to calculate the ozone optical depth were based on ozonesonde measurements made during the cruise [*Thompson et al*., 2000] and, to fill in data gaps, TOMS level 3 data. The instrument was calibrated using a Langley plot approach [*Shaw*, 1983] by the manufacturer prior to the cruise and again at Mauna Loa 5 months after the cruise. Calibration constants for the five wavelengths differed by less than 0.9% between the two calibrations, which corresponds to approximately 0.01 in optical depth.

2.2. Simbad

The Simbad radiometer was designed to collect data on AOD and water-leaving radiance, the basic satellite ocean-color variables [*Schwindling et al*., 1998]. Radiance is measured in five spectral bands centered at 443, 490, 560, 670, and 870 nm, total field of view is 3°, spectral bandwidth (FWHM) for each channel is 10 nm, and frequency of measurements is 10 Hz. In Sun-viewing mode the instrument functions like a standard sunphotometer, the only difference being that the optics are fitted with a vertical polarizer. This polarizer reduces reflected skylight and sunglint in the field of view when the instrument is operated in sea-viewing mode. The polarizer is not an issue for Sun intensity measurements because direct sunlight is not polarized. It takes 10 s to acquire a data set in Sun-viewing mode. Only the highest intensity during 1 s (i.e., out of 10 measurements) is stored automatically, to avoid pointing errors on a moving platform. Measurements were made systematically from the bow of R/V *Ron Brown* when the solar path was free of clouds, and repeated three times to reduce experimental errors.

Radiometric calibration was performed four times before and twice after the experiment at Stevenson Peak (1896 m), California, using the Bouguer-Langley method. No significant trend was detected in the calibration coefficients. Ln (E_o) and standard errors after correction for Earth-Sun distance are 12.656 ± 0.008, 13.014 ± 0.021, 12.906 ± 0.007, 12.920 ± 0.005, and 12.596 ± 0.008 at 443, 490, 560, 670, and 870 nm, respectively. The standard error is a measure of the expected error on aerosol optical thickness due to calibration for an air mass of unity. This error is inversely proportional to air mass. Except for the 490 nm spectral band, the standard error is below 0.01 in optical depth.

Errors in molecular optical depth and ozone absorption will reduce the accuracy of AOD retrievals. Also, some scattered light may reach the detectors because of the relatively large field of view (3°), artificially increasing atmospheric transmittance and thus decreasing AOD. A 1% error on the molecular optical depth at standard pressure and a 10 hPa error on surface pressure would give for an air mass of 1 a 0.005 error in AOD at 443 nm, decreasing to practically zero at 870 nm. To compute ozone absorption, vertical ozone amount was taken from ozonesondes deployed during the cruise [*Thompson et al*.,

2000]. A 10% error in ozone amount would translate into optical depth errors of 0.003 at 560 nm and 0.001 at 670 nm, and negligible (or nil) in the other spectral bands. These errors, computed for an air mass of unity, increase with air mass. Regarding scattered light, contamination is small in the presence of continental aerosols (i.e., <0.001 and 0.003 at 443 nm for an optical thickness of 0.05 and 0.2, respectively), but may be 5 to 10 times larger in the presence of maritime aerosols, due to the more pronounced forward peak of the phase function. Although some errors may compensate, the absolute error in AOD is probably of the order of 0.02 (0.03 at 490 nm). Since the absolute error is independent of optical depth, the relative error is inversely proportional to optical depth and becomes very large at low AOD (e.g., about 50% at 443 nm for an optical depth of 0.04).

2.3. Fast-Rotating Shadowband Radiometer

A shadowband radiometer measures the diffuse and global (upper hemispheric) irradiance and computes E as the difference between the two. The device gets its name from the hemispherical metal strip that rotates around the detector (the shadowband) and blocks the direct solar beam to yield a signal that is from the sky only (after the effect of the arm is included).

The BNL fast rotating shadowband radiometer (FRSR) [*Reynolds et al*., 2001] is a marine-hardened adaptation of the multifrequency rotating shadowband radiometer (MFRSR) developed by *Harrison et al*. [1994]. The FRSR uses the same radiometer head, with seven independent interference-filter-photodiode detectors and an automated rotating shadowband technique to make spatially resolved measurements at seven wavelength passbands. The FRSR head has one broadband silicon detector and six 10-nm-wide channels at 415, 500, 610, 660, 870, and 940 nm. Modifications to the detector circuitry used for continental applications are necessary because the response time of the original circuitry is too slow for use on a moving ship. If the response time of the detector is too slow, wave action may cause the orientation of the radiometer to change appreciably during the time the shadowband is occulting the Sun. The rotation of the shadowband itself must be sufficiently fast for the same reason. The BNL marine version of the shadowband radiometer is hereafter referred to as the FRSR.

The shadowband radiometer must properly measure the global and diffuse irradiances from which the direct-beam irradiance is derived by the subtraction

$$E_H = E_G - E_D, \tag{4}$$

where E_H is the direct-beam irradiance projected onto a horizontal plane, E_G is the global irradiance on the horizontal plane, and E_D is the diffuse irradiance from nonforward scattering. The global irradiance E_G is measured when the band is out of the field of view and the sensor is exposed to full sunlight, while E_D is measured with the sensor shadowed by the band. The irradiance normal to the incident beam, E in (1), is computed by

$$E = E_H/\cos(\theta_s). \tag{5}$$

Corrections for the sky blocked by the occulting band and for roll and pitch of the sensor head are made and discussed in detail by *Reynolds et al*. [2001]. The instrument calibration coefficients for Aerosols99 were determined using the Langley technique at Mauna Loa. Additional calibrations were performed during the cruise that showed good agreement with the Mauna Loa data. The accuracy of the calibration coefficients is thought to be about 5%, and the accuracy of the irradiance measurements is about 6%. While the uncertainty in the AOD measurement also depends on the air mass, for typical conditions, measurements of the AOD of sea-salt aerosol (due to its low AOD) are the most uncertain.

Filtering the data stream to avoid clouds is the most important challenge for FRSR data processing. Because the FRSR operates autonomously, cloud observations are naturally part of the signal that must be processed to obtain τ. The cloud filter that is currently used is based on two steps: computing signal statistics over windows of periods of less than 2 hours and using these statistics to judge the quality of the observation under consideration. If the standard deviation of the observations in a 2-hour moving window is less than 0.05, a subjectively defined threshold, and the observation at the center of the window is also less than 0.05, the central observation is accepted. The underpinning of this cloud-filtering technique is that τ is relatively constant over a period of 2 hours, while the cloud signal is highly variable. This approach has proven relatively successful, although improvements in the filter are expected in the future. It should be noted here that Aerosols99 was the first deployment of the FRSR. In the 18 months since that cruise, substantial improvements in the FRSR and data processing techniques have been added.

2.4. Micropulse LIDAR

The Micropulse LIDAR (SESI, Burtonsville, Maryland) is a small compact LIDAR system which averages high-repetition, low-energy pulses to obtain a profile of attenuation/backscattering in the atmosphere [*Spinhirne et al*., 1995]. The Micropulse LIDAR used during the cruise operated at 523 nm, with a pulse repetition rate of 2500 Hz, the vertical resolution was 75 m, and data were collected to 30 km. During the day the signal above 10 km became increasingly noisy due to a combination of attenuation in the boundary layer and background sunlight at 523 nm, but during the night low noise data could be obtained to 20 km in the absence of clouds. The details of the algorithm to derive the AOD from the micropulse LIDAR are detailed elsewhere [*Welton*, 1998; E. J. Welton et al., Aerosol and cloud measurements using micropulse LIDAR systems, submitted to *Journal of Atmospheric and Oceanic Technology*, 2000, hereinafter referred to as Welton et al., submitted manuscript, 2000]. However, an overview of the technique will be presented here.

The basic equation governing LIDAR propagation, when the LIDAR is vertically oriented, is

$$Er(t) = CEo(\beta_r(180, z) + \beta_a(180, z)) \cdot \exp\left(-2\int_0^z [c_r(z') + c_a(z')]\,dz'\right)/z^2, \tag{6}$$

where Er is the received energy, Eo is the outgoing pulse energy, $\beta_r(180, z)$ is the Rayleigh (molecular) backscattering, $\beta_a(180, z)$ is the aerosol backscattering, c_r is the Rayleigh attenuation, c_a is the aerosol attenuation, and C is an instrument calibration constant. The time the signal is received is related to the altitude z by the time it takes for the LIDAR pulse to travel up to that altitude and back ($z = tc/2$, where c is the speed of light). By using time-resolved return signals,

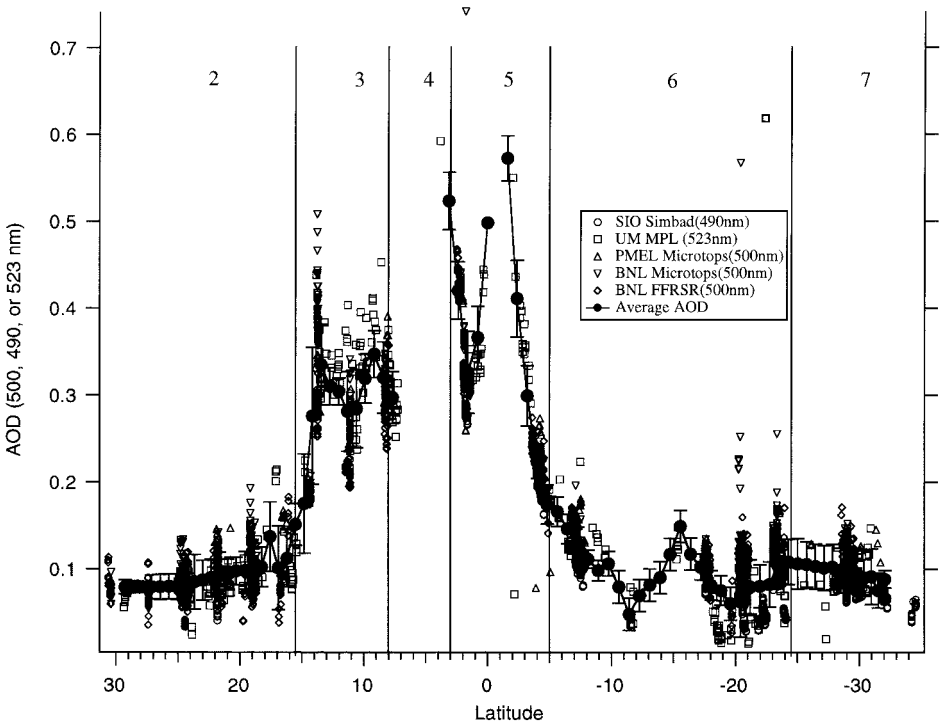

Figure 1. AOD at approximately 500 nm for each instrument and the average values. Error bars are displayed on the average values, derived from the standard deviation between the average and the measurements. Regions 2–7 are displayed on graph as discussed in section 3.2.

profiles of the backscattering and attenuation can be obtained. C contains information on system parameters such as throughput, solid angle acceptance of the receiver, divergence of the laser beam, and other parameters. While in principle this could be calculated [*Spinhirne et al.*, 1980], in practice it is much simpler and accurate to derive this parameter from measurements in the field, as will be discussed below. For a practical LIDAR system such as the MPL there are other important affects which must be taken into account, namely, the overlap function and afterpulse function. The overlap function describes the loss in signal strength at close range due to poor focusing to the detector by the MPL telescope and optical design at close range (less than 4 km). Signals greater than the overlap range are not effected by this problem. By making horizontal measurements in a horizontally homogenous atmosphere this overlap function can be determined and corrected. The afterpulse function is a result of cross talk between the laser pulse and detector, as well as dark noise in the system. Both of these effects were corrected for in this data set in the manner described by Welton et al. (submitted manuscript, 2000).

If the calibration coefficient is known, and a clean layer above the aerosol layer can be found where the backscattering and attenuation is dominated by Rayleigh scattering, then the returned energy from that altitude is simply

$$Er(t) = CEo\beta_r(180, z) \cdot \exp\left(-2 \int_0^z [c_r(z') + c_a(z')]\, dz' \right)/z^2 \quad (7)$$

or

$$Er(t) = CEo\beta_r(180, z) \cdot \exp\left(-2\,\mathrm{AOD} - 2 \int_0^z c_r(z')\, dz' \right)/z^2. \quad (8)$$

The later integral can be calculated, thus

$$\mathrm{AOD} = -\frac{1}{2} \ln\left[\frac{Er(t)z^2}{CEo\beta_r(180, z)} \right] - \int_0^z \mathrm{c_r}(z')\, \mathrm{d}z'. \quad (9)$$

The measurement of the AOD with the LIDAR only requires finding a clean layer above the aerosols and accurate calculation of the system calibration constant C. It is important to note that this product does not depend on any assumption of the extinction/backscatter ratio. The LIDAR AOD calculation has the advantage that for boundary layer aerosols, it is the only method that can determine the AOD during the night and in the presence of high cirrus. Care must be taken in determining the level chosen to represent a clean atmosphere above the aerosol Welton et al. (submitted manuscript, 2000). This is usually obvious from the range-corrected LIDAR signal by looking for a region for which $\ln [Er(t)z^2]$ is decaying at the rate appropriate for Rayleigh scattering.

When the AOD is known from independent measurements (such as with a handheld sunphotometer), the above equations can be turned around to determine the system calibration constant C. During this cruise, during cloud-free periods during the day, episodic measurements of the AOD were made with an independent Microtops sunphotometer (the data from this instrument are not included in this paper). Thus the calibration coefficient was determined at intervals throughout the

Table 1. AOD (500 nm) and α[a]

DOY	Latitude	AOD	s.d.	Angstrom	s.d.
18	29.27	0.08	0.01 (9)		
18.5	27.84	0.08	0.02 (42)	0.65	0.20 (20)
19	26.43	0.08	int		
19.5	25.05	0.08	0.02 (156)	0.32	0.17 (60)
20	23.68	0.08	0.01 (83)		
20.5	22.32	0.09	0.02 (129)	0.06	0.15 (8)
21	20.96	0.09	0.02 (34)		
21.5	19.61	0.10	0.03 (113)	0.21	0.29 (6)
22	18.25	0.10	0.02 (91)		
22.5	16.89	0.10	0.04 (44)	−0.25	0.17 (20)
23	15.52	0.15	0.04 (18)		
23.5	14.13	0.28	0.09 (104)	0.38	0.15 (29)
24	12.73	0.31	0.03 (15)		
24.5	11.31	0.28	0.05 (86)	0.18	0.11 (75)
25	09.87	0.32	0.05 (24)		
25.5	08.42	0.32	0.04 (85)	0.49	0.11 (34)
26	06.94	0.29	0.02 (17)		
27.5	2.37	0.42	0.09 (173)	1.21	0.12 (90)
28	0.80	0.37	0.05 (41)		
29	−02.38	0.41	0.06 (12)		
29.5	−04.01	0.22	0.02 (296)	0.74	0.12 (265)
30	−05.64	0.17	0.02 (15)		
30.5	−07.28	0.13	0.02 (322)	0.70	0.31 (246)
31	−08.94	0.10	0.03 (7)		
31.5	−10.60	0.08	int		
32	−12.26	0.07	0.03 (6)		
32.5	−13.92	0.09	int		
33	−15.57	0.15	0.02 (6)		
33.5	−17.21	0.10	0.01 (138)		
34	−18.83	0.07	0.04 (22)		
34.5	−20.42	0.07	0.05 (283)	0.46	0.28 (183)
35	−21.99	0.08	0.04 (9)		
35.5	−23.52	0.11	0.02 (204)	0.32	0.20 (167)
36	−25.01	0.11	0.04 (2)		
36.5	−26.44	0.10	0.03 (2)		
37	−27.82	0.10	0.03 (10)		
37.5	−29.13	0.10	0.02 (300)	0.44	0.13 (250)
38	−30.37	0.09	0.02 (17)		
38.5	−31.52	0.07	0.02 (42)	0.28	0.08 (38)

[a]Data are given at midnight (for example, DOY 18) and noon UTC (for example, 18.5). Numbers of data points are given after the standard deviations; "int" means that no data exist in this period and value is an interpolation.

cruise. The calibration coefficient was fit to a linear equation and varied during the cruise by 20%. The accuracy of our calibration procedure is estimated to be ±3%, while the accuracy of the AOD calculation is affected by the calibration coefficient and the overlap and afterpulse corrections. The accuracy of the AOD determined from the LIDAR is estimated to be ±0.05.

2.5. Aerosol Regions

Aerosol regions were defined for the marine boundary layer (MBL) by surface trace gas concentrations, aerosol chemical and physical properties, and trajectories at the 500 m arrival height, [*Bates et al*., this issue]. These regions may be somewhat different than those defined by other methods such as vertical profiles with lidar or ozonesondes [*Thompson et al*., 2000]. By combining the surface information, seven separate MBL regions (regions 1–7) were defined on the basis of the chemical signatures: North American air mass (37°N–31°N), Northern Hemisphere clean (31°N–15.5°N), African dust (15.5°N–8°N), mixed dust and biomass burning (8°N–3°N), biomass burning (3°N–5°S), Southern Hemisphere clean (5°S–24.5°S), and South Atlantic temperate marine air mass (24.5°S–33°S).

2.6. Derivation of the Angstrom Exponent

Other than the LIDAR, all of the instruments measure the AOD at multiple wavelengths close to simultaneously. For each of these instruments, α was calculated using all the usable channels for that instrument (some channels in specific instruments were not calibrated well and were not included). The α was calculated by determining the least squares fit to the line

$$\ln(\mathrm{AOD}(\lambda)) = B - \alpha \ln(\lambda), \tag{10}$$

for each measurement set (a set being the available wavelengths for a single instrument at a given time). B is the intercept and is not used (it is equivalent to the fitted result for ln [AOD (1 nm)]. This was done throughout the data set for each instrument's AOD measurement.

2.7. Compilation of Averages for the Days

All the independent measurements of the AOD were compiled into a single data set as shown in Figure 1, choosing the AOD at the wavelength of each instrument closest to 500 nm. No effort was made to correct for the small wavelength differences between the instruments. The largest wavelength differ-

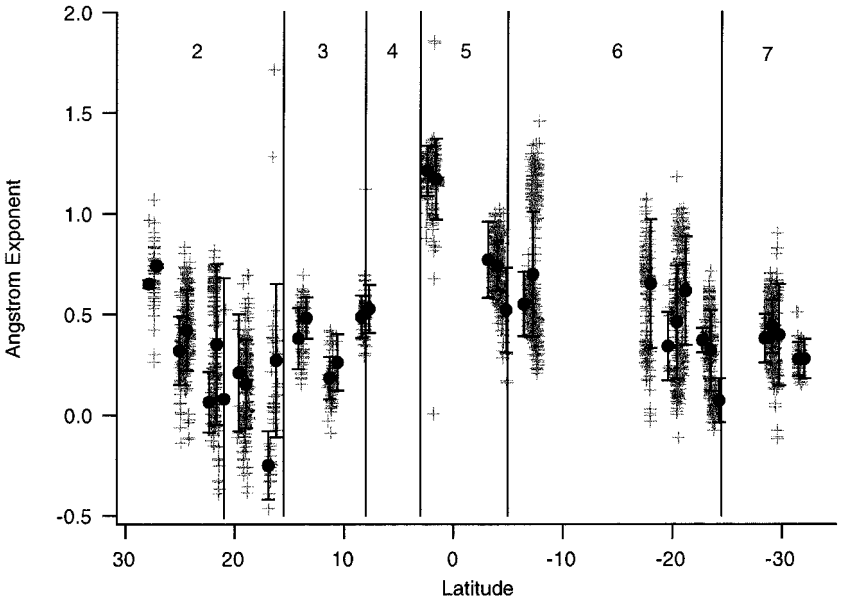

Figure 2. The variation in α throughout the cruise. Regions are displayed as in Figure 1. Average α and standard deviation between this average and the data are displayed.

ence was from 490 to 523 nm, and with the highest average α ($=1.2$) this is only a 5% effect. As can be seen, the AOD varied strongly throughout the cruise depending on the atmospheric influences. For comparison with the other data sets obtained, an average AOD and α for 1/4 day intervals during the cruise had to be determined. For region 4 and January 28, 1999, because of almost constant cloud cover, there was virtually no opportunity to measure the AOD with any technique. For the rest of the cruise the average AOD and α were calculated at 1/4 day intervals centered on midnight, 0600, 1200, and 1800 UTC.

To determine the average AOD for a period, a third-order polynomial was fit to 1.5 days of data centered on the desired time. This polynomial was then used to determine the average AOD for 1/4 day intervals and is shown in Figure 1. For noon and midnight (even and 0.5 day increments) the AOD is listed in Table 1. This method was chosen to provide a true time average during that period and to avoid biasing the average toward periods of many measurements. To get an estimate of the accuracy of these averages, the standard deviation of the difference between this average and the original data was determined. This standard deviation is shown in the figure as the error bars on the average AOD data, and in Table 1.

The α was determined by simply averaging the data during the relevant period, and is shown in Figure 2. We chose to do this, rather than the method chosen for AOD, because the differences between separate measurements of α appeared random. The errors bars on these graphs are determined by the standard deviation between this average and the original data. The α and standard deviation are also shown in Table 1. There are more periods without α data than for the AOD since there were times when only the LIDAR obtained AOD measurements (for example, at night), and the LIDAR does not obtain α.

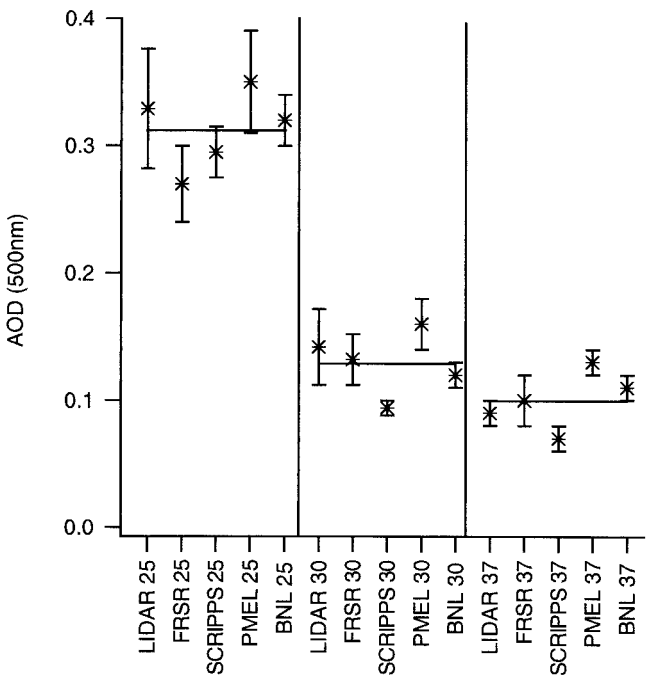

Figure 3. Comparison of the measured AOD (500 nm) between independently calibrated instruments for 3 days, day of year (DOY) 25, 30, and 37. Each instrument's average measurement for the period is displayed, along with the standard deviation. The line in each segment is the average of all the instruments for that day.

3. Results and Discussion

We will first look at a comparison of the different instruments, then look at specific regions of the cruise.

3.1. Instrument Comparison

To investigate the variation in measurements between the different instruments, we looked at 3 different days when the AOD appeared stable throughout the day. We chose to do this so that we could get representative samples of each instrument.

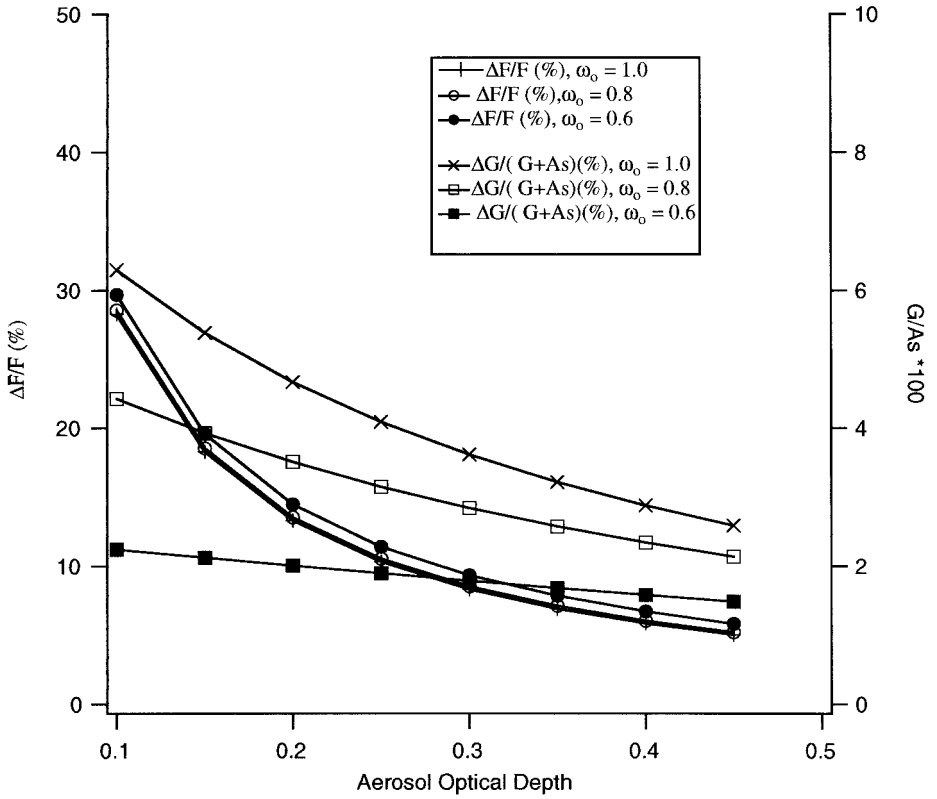

Figure 4. Error in calculated forcing with ΔAOD = 0.03 versus AOD. Also displayed is the fractional error in the total (surface plus aerosol) reflectance due to this 0.03 error in AOD. In the calculation, $\mu_0 = 0.8$, $\beta = 0.3$, and $A_s = 0.1$.

It was difficult to find a time when all the instruments were working at exactly the same time because the handheld sunphotometers were most active at noon when the LIDAR was turned off because of the low solar zenith angle. The three periods chosen were day of year (DOY) 25, 30, and 37 (this corresponds to latitude ranges of 9.8°N–6.9°N, 5.6°S–8.9°S, and 27.8°S–30.4°S, respectively).

Figure 3 shows the comparison between the instruments. In this figure the AOD (500 nm) is displayed for each instrument along with the standard deviation for the individual instrument. We also show the average of the measurements during each day. The averages and standard deviations for each day are 0.31 ± 0.03, 0.13 ± 0.02, and 0.10 ± 0.02. It is interesting that the more standard handheld sunphotometers (the Scripps Simbad and the BNL and PMEL Microtops) had a constant difference (to within ±0.01) between them, as would be expected with small calibration offsets. The relationship between these instruments and the nontraditional LIDAR and FRSR varied between the days chosen, however. It should be pointed out that the LIDAR and FRSR were averages over longer periods (throughout the day for the LIDAR and during daylight with the FRSR), but overall the instruments agreed fairly well.

Table 2. AOD and α Broken Down by Region

Region	AOD	s.d.	α	s.d.
2	0.09	0.02	0.27	0.28
3	0.29	0.05	0.36	0.13
4	0.41	0.16	0.52	
5	0.36	0.13	0.88	0.30
6	0.10	0.03	0.45	0.20
7	0.10	0.01	0.35	0.07

This uncertainty may affect the predictions of radiative forcing. In cloud-free regions the direct radiative forcing due to aerosols can be expressed as [e.g., *Iacobellis et al.*, 1999]

$$F = \mu_0 E_0 T_a^2 G \tag{11}$$

with

$$G = R + T^2 A_s/(1 - A_s R) - A_s \tag{12}$$

$$R = \omega_o \beta[1 - \exp(-\mathrm{AOD}/\mu_0)] \tag{13}$$

$$T = \exp(-\mathrm{AOD}/\mu_0) + \omega_o(1 - \beta)[1 - \exp(-\mathrm{AOD}/\mu_0)], \tag{14}$$

where μ_0 is the Sun zenith angle, E_0 is the extraterrestrial solar flux, T_a is the transmittance of the atmosphere above the aerosols, A_s is the albedo of the underlying surface, R and T are the fraction of sunlight scattered and transmitted by the aerosol layer, respectively, ω_o is the single scattering albedo of aerosols, and β is the fraction of scattering by aerosols which goes upward.

The relative error on F, $\Delta F/F$, due to error on AOD, ΔAOD, can be estimated from (11) as

$$\Delta F/F \approx (1/G)(\partial G/\partial \mathrm{AOD})\Delta\mathrm{AOD}. \tag{15}$$

Figure 4 displays $\Delta F/F$ as a function of AOD for $\mu_0 = 0.8$, $\beta = 0.3$, $A_s = 0.1$, ΔAOD = 0.03, and three values of ω_o from 1 (nonabsorbing aerosol) to 0.6 (absorbing aerosol). Also in Fig-

ure 4 we show the ratio of $\Delta G/(G + A_s)$, which is effectively the error in reflectance/(total reflectance), as a function of AOD and ω_o. At small AOD (0.1), $\Delta F/F$ is practically equal to ΔAOD/AOD and is only weakly dependent on ω_o. Because the aerosol adds little at low AOD, the error in the combined surface/aerosol reflectance is less than 6% in all cases.

3.2. Specific Regional Analysis

We will now discuss the individual regions. These regions are shown in Figures 1 and 2 as regions 2–7. The AOD and α with their associated standard deviations are detailed in Table 2. In region 1 there were very few AOD measurements because of clouds and rain. The other regions will now be discussed.

3.2.1. Region 2: North Atlantic marine air mass (31°N–15.5°N). In this region the calculated 6-day back trajectories [*Bates et al*., this issue] were mostly over the open ocean. This area was characterized by a very clean atmosphere (AOD = 0.09 ± 0.02). The α was also low (0.27 ± 0.27) indicating a dominance by large particles. While the AOD measured by all instruments were fairly consistent, α had large variation. To some extent, this is because at low AOD, α is difficult to determine and very dependent on the accuracy of the individual instruments absolute calibration.

3.2.2. Region 3: African dust air mass (15.5°N–8°N). In this region the chemical signature of the surface aerosols and the back trajectories indicated that the major source of the aerosols was northwest African dust. The AOD was highly variable and increased; the average AOD was 0.29 (±0.05). The α remained low (0.36 ± 0.13), as seen previously in dust aerosols [*Welton*, 1998; *Smirnov et al*., 1998]. The variability in α between instruments was much lower with the increased AOD, indicating that much of the earlier variability was probably caused by small calibration errors in the individual instruments' Eo.

3.2.3. Region 4: Mixed African dust and biomass burning (8°N–3°N). This region was the beginning of the ITCZ. The other cruise data characterized the aerosols as mixed, but with almost continuous boundary layer clouds, thus there were virtually no AOD measurements in this region.

3.2.4. Region 5: Biomass burning in the ITCZ (3°N–5°S). This region had the largest values and range of AOD. The AOD was 0.36 ± 0.13. Figure 1 shows the large excursions in the AOD experienced in this region. The α was much larger (0.88 ± 0.30) indicating a dominance by small particles. The calculated back trajectories indicated that the source of the aerosol was burning regions in southwestern North Africa [*Bates et al*., this issue]. After a peak at the equator, the AOD slowly decreased as we moved south.

3.2.5. Region 6: South Atlantic tropical marine air mass (5°S–24.5°S). In this region the surface concentrations of ozone and CO reached clean Southern Hemisphere levels [*Thompson et al*., 2000]. However, the AOD measurements indicated upper level aerosols. This was confirmed in the LIDAR profile data [*Voss et al*., this issue]. The average AOD in this region was low (0.10 ± 0.03); however, there was definite structure to the AOD with change in latitude. The α decreased from its high in region 5 to 0.45 ± 0.20; however, it had not decreased to the levels seen in the Northern Hemisphere marine air mass of region 2.

3.2.6. Region 7: South Atlantic temperate marine air mass (24.5°S–33°S). At this point the air mass trajectories indicated that the aerosols were advected from the South Atlantic. Average AOD values were similar to the Northern Hemisphere clean values (region 2) (0.10 ± 0.01), with α also similar to region 2 (0.35 ± 0.07).

4. Conclusion

This 25-day cruise afforded the opportunity to sample a variety of aerosol regions with an extensive set of chemical, physical, and optical instrumentation. The AOD and α measured with the variety of instruments and techniques agreed fairly well and afforded an opportunity to compare the various techniques. The handheld sunphotometers and the FFRSR allowed the AOD and α to be measured during completely cloud-free periods. The FFRSR, with the automatic sampling, could measure the AOD during any daytime cloud-free period, but then depended on postprocessing to select valid measurements. The operators of the handheld instruments could select cloud-free periods to measure, but obviously would not make measurements continuously throughout the day. The LIDAR could obtain boundary layer AOD during the night and in periods of high cirrus but only at one wavelength, so it could not provide any measure of α. However, the extinction/backscattering parameter, derived from the LIDAR inversion, is related to the size distribution [see *Voss et al*., this issue]. Each instrument has its own advantages and disadvantages, but the combination of the techniques allows a more complete data set to be obtained.

Acknowledgments. We thank the officers and crew of the NOAA Research Vessel *Ron Brown*. We would like to acknowledge the support of NASA under contract NAS5-31363 (K. J. V. and E. W.), NAS5-97135 (R. F.), and SIMBIOS 52-210.91 (M. M. and R. M. R.). Part of this work (P. K. Q.) was funded by the Aerosol Program of the NOAA Climate and Global Change Program.

References

Angstrom, A., The parameters of atmosphere turbidity, *Tellus*, *16*, 64–75, 1964.

Bates, T. S., P. K. Quinn, D. J. Coffman, J. E. Johnson, T. L. Miller, D. S. Covert, A. Wiedensohler, S. Leinert, A. Nowak, and C. Neus, Regional physical and chemical properties of the marine boundary layer aerosol across the Atlantic during Aerosols99: An overview, *J. Geophys. Res*., this issue.

Bucholtz, A., Rayleigh-scattering calculations for the terrestrial atmosphere, *Appl. Opt*., *34*, 2765–2773, 1995.

Harrison, L., J. Michalsky, and J. Berndt, Automated multi-filter rotating shadowband radiometer: An instrument for optical depth and radiation measurements, *Appl. Opt*., *33*, 5126–5132, 1994.

Iacobellis, S. F., R. Frouin, and R. C. J. Somerville, Direct radiative forcing by biomass-burning aerosols: Impact of correlations between controlling variables, *J. Geophys. Res*., *104*, 12,031–12,045, 1999.

Kasten, F., and A. T. Young, Revised optical air mass tables and approximation formula, *Appl. Opt*., *28*, 4735–4738, 1989.

Mueller, J., C. McClain, R. Caffrey, and G. Feldman, The NASA SIMBIOS Program, *Backscatter*, *9*(2), 29–32, 1998.

Penndorf, R., Tables of refractive index for standard air and the Rayleigh scattering coefficient for the spectral region between 0.2 and 20 um and their application to atmospheric optics, *J. Opt. Soc. Am*., *47*, 176–182, 1957.

Quinn, P. K., D. J. Coffman, T. S. Bates, T. L. Miller, J. E. Johnson, K. J. Voss, E. J. Welton, and C. Neususs, Dominant aerosol chemical components and their contribution to extinction during the Aerosols99 cruise across the Atlantic, *J. Geophys. Res*., this issue.

Reynolds, R. M., M. A. Miller, and M. J. Bartholomew, Design, operation, and calibration of a shipboard fast-rotating shadow-band spectral radiometer, *J. Atmos. Oceanic Technol*., *18*, 200–214, 2001.

Schwindling, M., P.-Y. Deschamps, and R. Frouin, Verification of aerosol models for satellite ocean color remote sensing, *J. Geophys. Res*., *103*, 24,919–24,935, 1998.

Shaw, G. E., Atmospheric ozone: Determination by Chappuis band absorption, *J. Appl. Meteorol*., *18*, 1335–1339, 1979.

Shaw, G. E., Sun photometry, *Bull. Am. Meteorol. Soc*., *64*, 4–9, 1983.

Smirnov, A., B. N. Holben, I. Slutsker, E. J. Welton, and P. Formenti, Optical properties of Saharan dust during ACE 2, *J. Geophys. Res*., *103*, 28,079–28,092, 1998.

Spinhirne, J. D., J. A. Reagan, and B. M. Herman, Vertical distribution of aerosol extinction cross section and inference of aerosol imaginary index in the troposphere by LIDAR technique, *J. Appl. Meteorol*., *19*, 426–438, 1980.

Spinhirne, J. D., J. Rall, and V. S. Scott, Compact eye-safe LIDAR systems, *Rev. Laser Eng*., *23*, 26–32, 1995.

Thompson, A. M., B. G. Doddridge, J. C. Witte, R. D. Hudson, W. T. Luke, J. E. Johnson, B. J. Johnson, S. J. Oltmans, and R. Weller, A tropical Atlantic paradox: Shipboard and satellite views of a tropospheric ozone maximum and wave-one in January–February 1999, *Geophys. Res. Lett*., *27*, 3317–3320, 2000.

Voss, K. J., E. J. Welton, J. Johnson, A. Thompson, P. Quinn, and H. Gordon, Lidar measurements during Aerosols99, *J. Geophys. Res*., this issue.

Welton, E. J., Measurements of aerosol optical properties over the ocean using sunphotometry and LIDAR, Ph.D. dissertation, Univ. of Miami, Coral Gables, Fla., 1998.

R. Frouin, Scripps Institution of Oceanography, University of California, San Diego, La Jolla, CA 92037.

M. Miller and R. M. Reynolds, Environmental Sciences Department, Brookhaven National Laboratory, Upton, NY 11973.

P. K. Quinn, Pacific Marine Environmental Laboratory, NOAA, Seattle, WA 98115.

K. J. Voss (corresponding author), Department of Physics, University of Miami, Miami, FL 33146. (voss@physics.miami.edu)

E. J. Welton, Goddard Earth Science and Technology Center, University of Maryland, Baltimore, MD 21228.

(Received July 6, 2000; revised September 22, 2000;
accepted November 1, 2000.)